



Analysis of SPMSMs with Outer Rotor Configuration by Analytical Model and Finite Element Technique

Hoang Bui Huu¹, Viet Nguyen Nga², Dinh Bui Minh², Bao Doan Thanh³, Vuong Dang Quoc^{2*}

¹ Faculty of Electrical Engineering - Automation, University of Economics, Technology for Industries, Hanoi 100000, Vietnam

² School of Electrical and Electronic Engineering, Hanoi University of Science and Technology, Hanoi 100000, Vietnam

³ Faculty of Engineering and Technology, University of Quy Nhon, Quy Nhon City 55100, Vietnam

Corresponding Author Email: vuong.dangquoc@hust.edu.vn

Copyright: ©2024 The authors. This article is published by IETA and is licensed under the CC BY 4.0 license (<http://creativecommons.org/licenses/by/4.0/>).

<https://doi.org/10.18280/jesa.570405>

ABSTRACT

Received: 29 February 2024

Revised: 15 May 2024

Accepted: 24 May 2024

Available online: 27 August 2024

Keywords:

surface-mounted-permanent magnet synchronous motor, outer rotor configuration, analytical method, finite element technique

In this study, a surface mounted-permanent magnet synchronous motor (SPMSM) with outer rotor configuration applied to the fields of industry and electric drive is proposed by an association between the analytical model and finite element technique. Firstly, the methodology involves a detailed development of the analytical calculation to compute crucial parameters for the SPMSM. Next, a finite element technique is proposed to validate the analytical parameters and simulate various aspects such as the magnetic flux density, output torque, cogging torque, torque ripple, back electromotive force, flux linkage and temperature rise. The developed methods are tested and validated on a practical problem involving a 7.5kW SPMSM with outer rotor type.

1. INTRODUCTION

Over the decades, the world has confronted various environmental challenges, notably global warming and air pollution. One significant contributor to air pollution is the use of fossil fuels in vehicles, emitting harmful gases. Beyond environmental concerns, issues like traffic congestion and soaring oil prices have prompted nations to explore alternative, eco-friendly transportation modes, with electric vehicles (EVs) emerging as a viable solution. Among the spectrum of EVs, the electric bicycle stands out as a suitable option for short-distance travel due to its attractive attributes such as affordability, ease of riding, convenient parking, health benefits, and environmental friendliness [1-4]. The motor for EVs plays a pivotal role, demanding careful design to ensure high efficiency, torque, and minimal noise.

In recent years, designers and researchers have scrutinized various motor types to identify the most efficient ones for powering EVs. Commonly employed motors for such applications include the switched reluctance motor (SRM), permanent magnet flux-switched motor (PMFSM), multi-flux permanent magnet (MFPM), permanent magnet synchronous motor (PMSM) and synchronous reluctance motor (SynRM) [5-10]. These motors have some advantages such as compact size and light weight due to the absence of brushes in their design. The rotor design of EV motors typically falls into two categories: those with an outer rotor, fitting between the two cranks and chain wheel, and those with an outer rotor, fitting into the wheel. Manh et al. [5] proposed various permanent magnet layouts in the rotor of the line-start permanent magnet assistance synchronous reluctance motor to mitigate this

drawback. The finite element method is used to study the V magnet form while accounting for skewed slots, demagnetization effect, and short circuit current. Feng et al. [6] primarily examined how the air-gap flux density, cogging torque, back electromagnetic force (EMF), and stator loss are affected by the rotor's dynamic eccentricity. It has a specific reference value for researching the low-speed high-torque PMSM rotor eccentricity. Lin et al. [7] proposed a 3-phase, external-rotor SRM that is intended for use in e-bike applications. It features 10 rotor poles and 6 stator poles. The bicycle kinematics are evaluated before beginning the SRM design and simulation. The machine's major dimensions and output power equation are determined analytically, and then a thorough finite element analysis (FEA) is conducted. In the study [8], the design of an electric bicycle axial-field permanent magnet (PM) brushless DC motor drive was presented. There are specifications for both the electronic converter and the motor. A brief discussion of the FEA was given for performance analysis. To confirm the real performance, a prototype motor was built. A strong correlation has been observed between the theoretical and experimental outcomes. Test findings verified that the suggested motor design was feasible. Huang [9] reviewed and compared various types of PM machines, including single and multiple rotor PM machines, radial, axial, and transverse flux PM machines, concentrated and distributed PM machines, electrically excited synchronous machines and reluctance machines, and exterior and interior rotor PM machines. Jung et al. [10] offered a comparative analysis of the features of bar-type interior PMSM and surface-mounted PMSM (SPMSM). The identical stator shape, rated speed, number of turns,

winding parameters, voltage limit, and magnet usage are configured in a pole/slot combination of six poles and 27 slots in order to perform characteristic analysis. Jusoh et al. [11], compared the inner and outer rotor designs of a single-phase PM flux switching machine with 8S-10P that was created especially for an electric bicycle. Using 2D-FEA, the machine performance was verified. The obtained result showed that the torque of the outer rotor is roughly 54.2% that of the inner rotor PMFSM.

Although many authors have researched the PMSMs as analyzed above. However, detailing the analytical calculation process to determine the required parameters of a synchronous motor is still a challenge that not many authors have mentioned.

In this paper, the required parameters of the SPMSM with outer rotor configuration as illustrated in Figure 1 is first designed by an analytical approach. Then, the FEA is presented to verify output parameters and simulate the magnetic flux density, torque, cogging torque, torque ripple, back EMF, flux linkage and temperature rise. The development of these methods will be validated on a 7.5kW SPMSM with outer rotor structure.

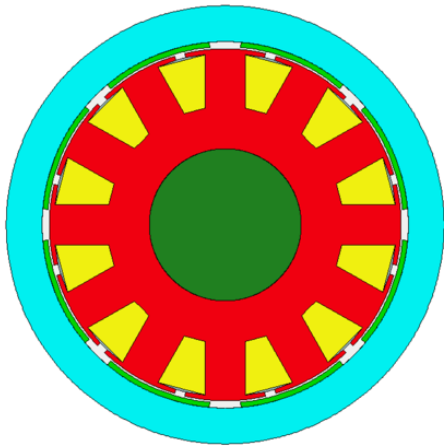


Figure 1. SPMSM with outer-rotor configuration

2. ANALYTICAL DESIGN

In this section, it provides a detailed presentation of the analytical design for the SPMSM with outer rotor type. The input parameters for this machine are given in Table 1.

Table 1. Input parameters of SPMSM with outer rotor configuration

No.	Description	Value	Unit
1	Input power (P_{rated})	7,5	kW
2	Rated voltage (U_{rated})	380	V
3	Efficiency (η)	93	%
4	Frequency (f_{rated})	50	Hz
5	Power factor ($\cos\phi$)	0.9	0.9
6	Number of pole pairs (p)	4	pairs
7	Phase number (m)	3	phase
8	Speed of rotor (n)	750	rpm

2.1 Design of stator

The outer diameter of stator is defined via the inner diameter of rotor (D_{ir}), air gap thickness (g) and the PM thickness (d_m),

i.e., [9, 10, 12]:

$$D_{os} = D_{ir} - 2(g + d_m), \quad (1)$$

The parameter D_{ir} is determined as [9, 12]:

$$D_{ir} = \left(\frac{V_r \cdot 4}{\pi \cdot k_{shape}} \right)^{\frac{1}{3}}, V_r = \frac{0.5 \cdot M_{rated} \cdot k_{safe}}{\sigma_m}, \quad (2)$$

where, V_r is the volume of stator and k_{shape} is the shape factor ($k_{safe} = 2 - 3$) [9], σ_m is the maximum stress and M_{rated} is the rated torque.

The PM thickness (d_m) is computed via the following parameters [12]:

$$d_m = \frac{\mu_r \cdot g}{\frac{B_r}{B_{g0}} - 1}, \quad (3)$$

where, μ_r is the relative permeability of PM, B_r is the remanent PM and B_{g0} is the magnetic flux density at the air gap. The stator length (L_{act}) is defined as:

$$L_{act} = \frac{D_{ir}}{k_{shape}}. \quad (4)$$

Via the term D_{ir} given in the Eq. (2), the width of each PM pole (w_p) is defined as:

$$w_p = \frac{D_{ir} \cdot \pi}{p}. \quad (5)$$

The width of PM (w_m) is calculated via the electrical angle of the PM (α), i.e.,

$$w_m = \frac{2\alpha \cdot w_p}{\pi} \quad (6)$$

Finally, the magnetic flux (ϕ_m) of the PM is defined as:

$$\phi_m = B_m \cdot w_m \cdot L_{act} \quad (7)$$

The magnetic flux on the tooth (ϕ_t) and the width of tooth (w_t) are respectively defined as:

$$\phi_t = \frac{\phi_m \cdot 2p}{Q}; w_t = \frac{\phi_t}{L_{act} \cdot k_{stack} \cdot B_t}, \quad (8)$$

where, Q is the number of slots, k_{stack} is the pressed factor of the stator yoke. The large diameter (b_1) and small diameter (b_2) of stator are calculated as:

$$b_1 = \frac{\pi \times (D_{os} - 2(h_w + h_{s0}))}{Q} - w_t, \quad (9)$$

$$b_2 = \sqrt{\frac{b_1^2 - 4\pi \times A_{slot}}{Q}}, \quad (10)$$

where, A_{slot} is the slot area. The height of stator slot is finally defined via the b_1 and b_2

$$h_s = \frac{2A_{slot}}{b_1 + b_2} \quad (11)$$

2.2 Design of outer rotor structure

In convention, the lengths of rotor yoke (L_{ry}) and stator yoke (L_{sy}) are defined as [9-12]:

$$L_{ry} = \frac{B_m \times w_m}{2B_{ry}}; L_{sy} = \frac{B_m \times w_m}{2B_{sy}} \quad (12)$$

where, B_{ry} and B_{sy} are the magnetic fluxes on the rotor and stator teeth, respectively. Finally, the outer diameter of the rotor is determined via the inner diameter and rotor length:

$$D_{or} = D_{ir} + L_{ry} \quad (13)$$

2.3 Design of windings

The winding factor (k_{dq}) is chosen following to Figure 2. The area of the winding (S_d) is calculated as [9]:

$$S_d = \frac{I_p}{J \cdot a} \text{ and } d = \sqrt{\frac{4 \cdot S_d}{\pi \cdot b}} \quad (14)$$

where, I_p is the phase current, J is the electric current density and a is the number of parallel branches. The number of turns is then calculated as:

$$n_s = \frac{1,1 \cdot U_p}{2\sqrt{2} \cdot \pi \cdot f_s \cdot q \cdot k_{dq} \cdot B_g \cdot \cos\gamma \cdot D_{ir} \cdot L_{act}}, \quad (15)$$

where, γ is the torque angle and k_{dq} is the winding factor.

Slot number	Pole number							
	4	6	8	10	12	14	16	20
6	0.866	0.866	0.500	0.500	0.866	0.866		
9		0.866	0.945*	0.945*	0.866	0.617	0.328	0.328
12			0.866	0.933	0.933	0.866		
15				0.866	0.951*	0.951*	0.866	
18					0.866	0.902	0.945	0.945
21						0.866	0.890	0.953*
24							0.866	0.933
27								0.877
30								0.866
33								
36								

$q > 0,5$

Slot number	Pole number							
	22	24	26	28	30	32	34	42
6	0.500		0.500	0.866		0.866	0.500	
9	0.617	0.866	0.949	0.949	0.866	0.617	0.328	0.866
12	0.250		0.25			0.866	0.933	
15	0.621		0.39					
18	0.902	0.866	0.647					
21	0.953*		0.89	0.866				
24	0.949		0.949	0.933		0.866	0.760	
27	0.915	0.945	0.954	0.954	0.945	0.915	0.877	
30	0.874		0.936	0.951		0.951	0.936	
33	0.866		0.903	0.928		0.954	0.945	
36			0.866	0.867	0.902	0.933	0.945	0.953

Figure 2. Winding factor (k_{dq}) [9]

The diagram of stator windings and cross-section of the motor is pointed out in Figure 3. Based on the development of the analytical theory, the results are given in Table 2.

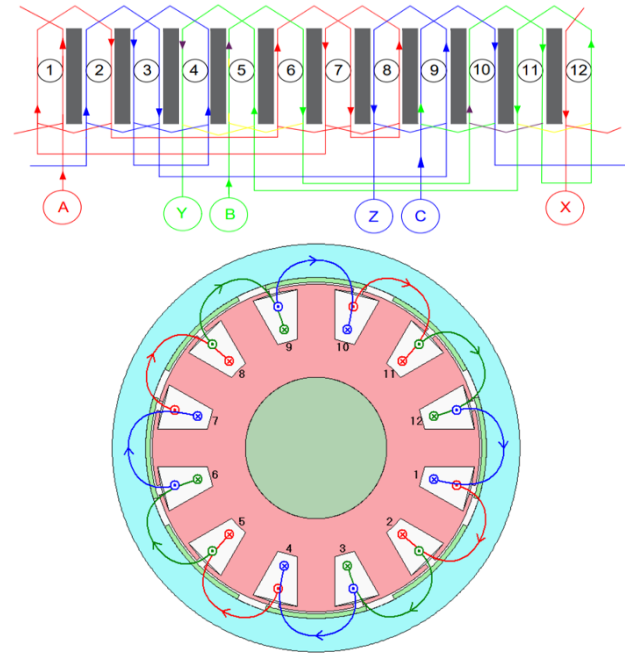


Figure 3. Diagram of stator windings (top) and cross-section of the motor (bottom)

Table 2. Analytical results

Description	Value	Unit
Outer diameter of stator	171	mm
Inner diameter of stator	73.5	mm
Outer diameter of rotor	212.95	mm
Inner diameter of rotor	178	mm
Length of stator	178	mm
Number of stator slots	10	Rănh
Air gap	1	mm
Thickness of PM	2.5	mm
Efficiency	94.016	%
Torque	95.839	Nm
Power factor	0.943	
Output Power	7527.2	W
Total Losses (on load)	479.12	W

3. FINITE ELEMENT ANALYSIS

In this part, the FEA is developed to verify main parameters obtained from the analytical model as presented in Section II. The Maxwell's equations and constitutive laws are expressed in Euclidean space \mathbb{R}^3 [9, 13-19]:

$$\text{rot } H = J_s, \quad \text{rot } E = -j\omega B, \quad \text{div } B = 0, \quad (16)$$

$$B = \mu H, \quad J = \sigma E, \quad (17)$$

where, J_s is the current density (A/m^2), H is the magnetic field (A/m), E is the electric field (V/m), B is magnetic flux density (T), J_{eddy} is the eddy current density (A/m^2), μ and σ are respectively the relative permeability and electric conductivity (S/m) and n is the unit normal exterior to Ω (with $\Omega = \Omega_c \cup \Omega_c^c$).

The above Eq. (17) is solved with boundary conditions (BCs) [9]:

$$n \times H|_{\Gamma_h} = 0, \quad n \cdot B|_{\Gamma_e} = 0, \quad (18)$$

Based on the Eqs. (17) and (18), the electromagnetic field equation written in Ω (domain of a PM machine) can be expressed as [9, 13-19]:

$$\text{rot} \left[\frac{1}{\mu} (\text{rot } \mathbf{A} - \mathbf{B}) \right] + \sigma \partial_t \mathbf{A} = \mathbf{J}_s - \sigma \text{grad} \phi. \quad (19)$$

The linkage flux (ϕ) is then defined as:

$$\phi = \frac{L}{S} \left(\iint_{\Omega^+} \mathbf{A} d\Omega - \iint_{\Omega^-} \mathbf{A} d\Omega \right), \quad (20)$$

where, L is the conductor length and S is the cross section area of the L . Based on the linkage flux as in the Eq. (21), the back EMF can be defined as:

$$e = - \frac{\partial \phi}{\partial t} \quad (21)$$

4. SIMULATION TEST

Based on the required parameters of the proposed motor from the analytical calculation given in Table 2, in this part, electromagnetic parameters is simulated and analyzed via the FEA. The model of 2D mesh for both stator and rotor is shown in Figure 4. The distribution of magnetic flux density in both stator and rotor is pointed out in Figure 5. The maximum value reaches 2.378T. The distribution of flux linkage is presented in Figure 6. It can be seen that it is very smooth and sinusoidal.

The waveform distribution of back EMF is illustrated in Figure 7. It can be observed that the waveform of back EMF is not sinusoidal with the high harmonic components. Figure 8 depicts the waveform of output torque. The maximum value is 112N.m and 74.5N.m for the average torque. Its torque ripple is indicated in Figure 9, with the value of under 3.5%. The torque ripple plays a crucial role in the design, and one major factor contributing to torque ripple is the cogging torque, as depicted in Figure 10. This result indicates the motor's stability and smooth operation, which are essential considerations in the overall design.

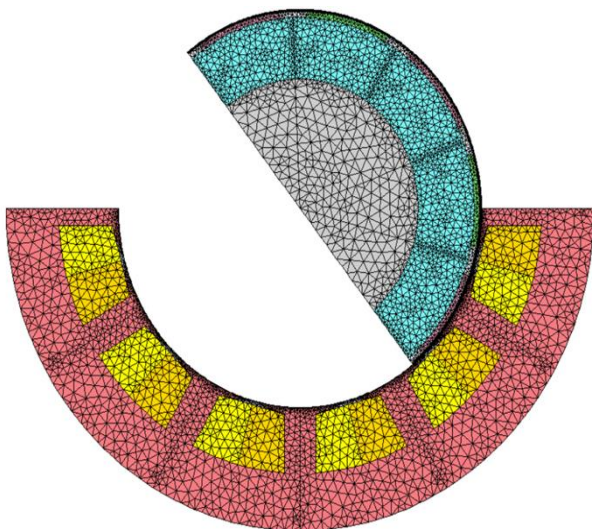


Figure 4. Model of 2D mesh

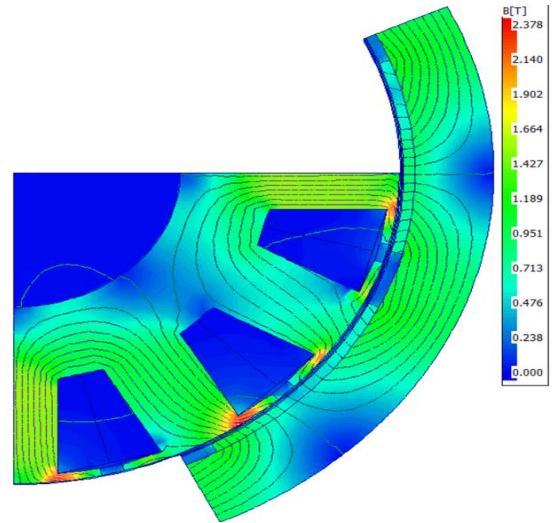


Figure 5. Distribution of magnetic flux density in both stator and rotor

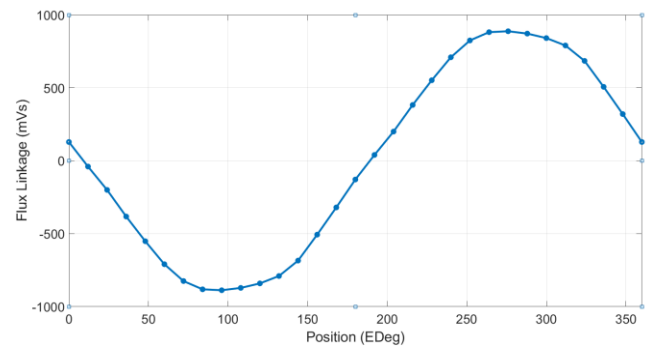


Figure 6. Distribution of waveform of linkage flux

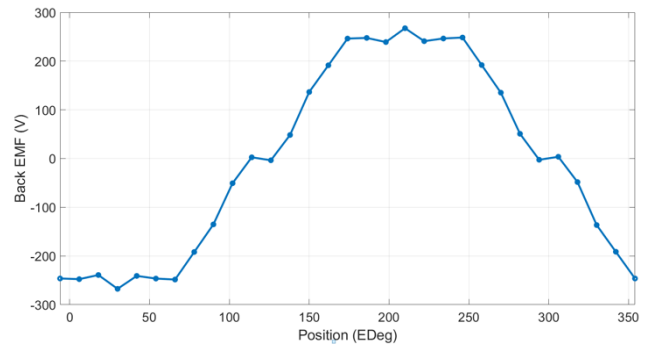


Figure 7. Distribution of waveform of back EMF

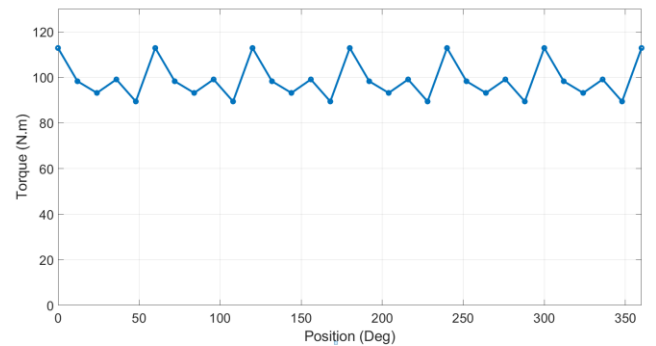


Figure 8. Distribution of waveform of output torque

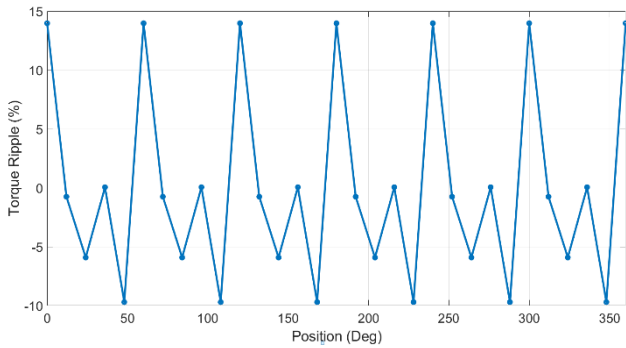


Figure 9. Distribution of waveform of torque ripple

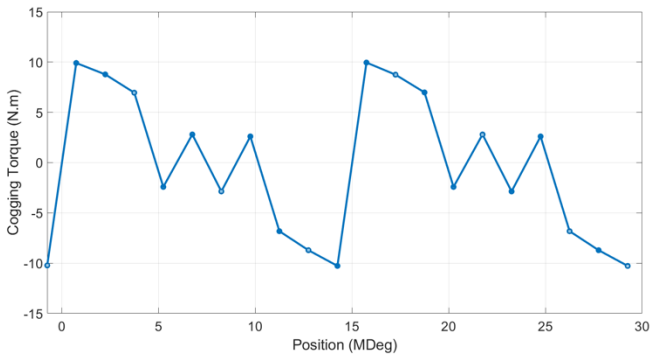


Figure 10. Cogging torque waveform

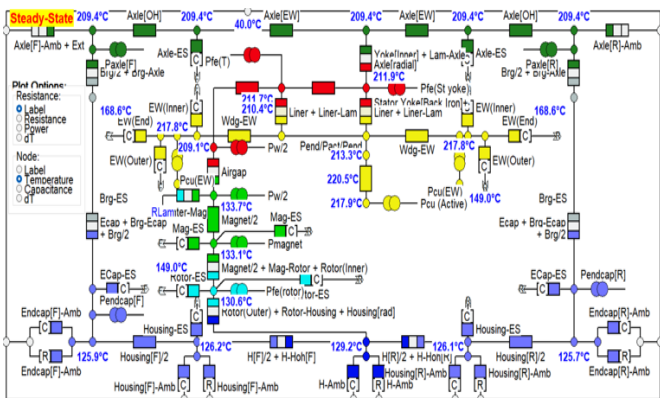


Figure 11. Thermal equivalent circuit diagram

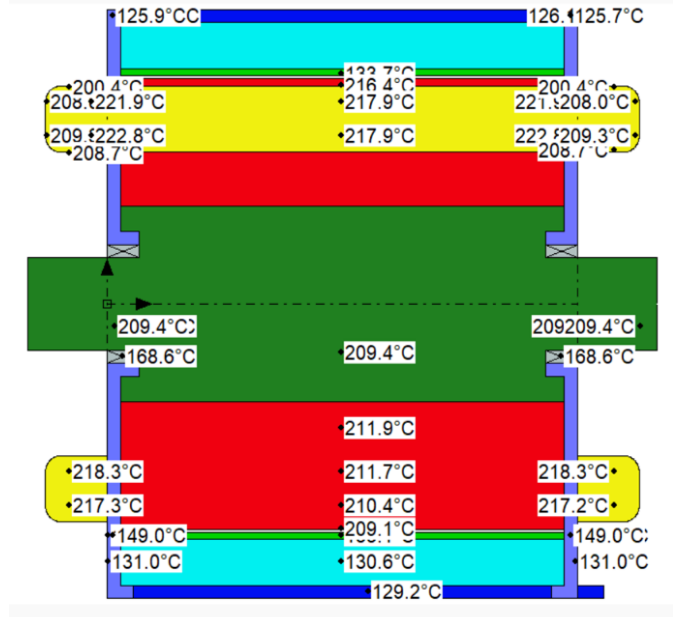
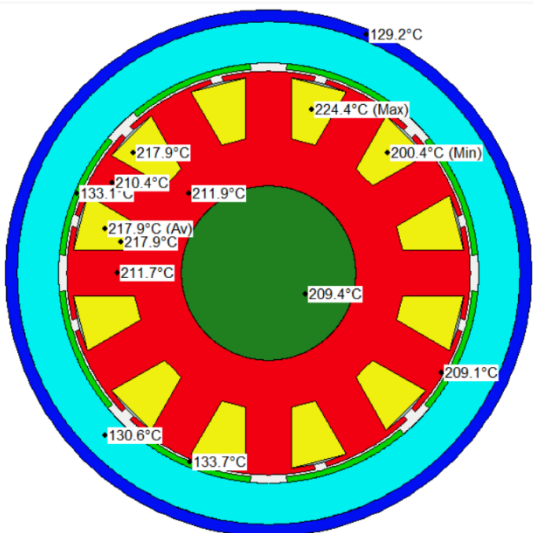


Figure 12. Radial (top) and axial (bottom) view results of the thermal model

Figure 11 presents the distribution of thermal equivalent circuit diagram with the heat distribution shown with corresponding temperature values in different colors. It can be seen that at the position of stator winding with yellow nodes and thermistors, the temperature in this area is larger than the remaining positions. The radial and axial results of the thermal model are illustrated in Figure 12. It can be seen that the maximum temperature is 224.4°C at the middle of the stator winding, and the minimum temperature is 129.2°C on the external surface of the stator and rotor yokes. For other areas such as the positions of stator and rotor yokes, the temperature rise has a trend of reduction. Through the map of temperature distribution, designers and manufacturers can give suitable solutions for cooling and insulation for the motor.

5. CONCLUSIONS

The SPMSM with outer rotor configuration of 7.5kW paper has successfully designed with the two processes: analytical calculation and FEA, where the analytic approach was proposed to defined required parameters of the proposed motor, and the FEA was then introduced to validate and simulate electromagnetic parameters, including magnetic flux density, linkage flux, back EMF, output torque, torque ripple and cogging torque. The achieved results have shown the working characteristics of the motor, especially the cogging torque and torque ripple values. These values will affect the motor's output torque and the vibration and noise of the motor under operation conditions. In addition, via the thermal equivalent circuit model, the temperature distribution at the different regions of the motor has also indicated. Finally, based on the obtained results, designers, researchers and manufacturers can be considered as a reference data to give the suitable prototype design of the SPMSM with outer rotor type.

This work facilitates the groundwork for future studies, potentially involving optimization methods like genetic algorithms and swarm optimization to refine design calculations.

REFERENCES

- [1] Taha, H.M., Alnaab, I. (2019). Designs of PMSMs with inner and outer rotors for electric bicycle applications. *Kurdistan Journal of Applied Research*, 4(1): 20-25. <https://doi.org/10.24017/science.2019.1.4>
- [2] Bhat, S.B., Nikam, S.P., Fernandes, B.G. (2014). Design and analysis of ferrite based permanent magnet motor for electric assist bicycle. In 2014 International Conference on Electrical Machines (ICEM), Berlin, Germany, pp. 106-111. <https://doi.org/10.1109/ICELMACH.2014.6960166>
- [3] Zhang, P., Sizov, G.Y., Demerdash, N.A. (2011). Comparison of torque ripple minimization control techniques in surface-mounted permanent magnet synchronous machines. In 2011 IEEE International Electric Machines & Drives Conference (IEMDC), Niagara Falls, ON, Canada, pp. 188-193. <https://doi.org/10.1109/IEMDC.2011.5994641>
- [4] Choi, J.Y., Park, H.I., Jang, S.M., Lee, S.H. (2011). Design and analysis of surface-mounted PM motor of compressor for electric vehicles applications according to slot/pole combinations. *The Transactions of the Korean Institute of Electrical Engineers*, 60(10): 1846-1857. <https://doi.org/10.5370/KIEE.2011.60.10.1846>
- [5] Manh, T.H., Minh, D.B., Minh, T.P., Quoc, V.D. (2023). Investigation of the influence of skewed slots and degmagnetization effects to line start permanent magnet assistance synchronous reluctance motors. *Engineering, Technology & Applied Science Research*, 13(1): 9807-9811. <https://doi.org/10.48084/etasr.5307>
- [6] Feng, L., Yu, S., Zhang, F., Jin, S., Sun, Y. (2022). Study on performance of low-speed high-torque permanent magnet synchronous motor with dynamic eccentricity rotor. *Energy Reports*, 8: 1421-1428. <https://doi.org/10.1016/j.egy.2022.03.018>
- [7] Lin, J., Schofield, N., Emadi, A. (2013). External-rotor 6-10 switched reluctance motor for an electric bicycle. *IECON 2013-39th Annual Conference of the IEEE Industrial Electronics Society*, Vienna, Austria, pp. 2839-2844. <https://doi.org/10.1109/IECON.2013.6699581>
- [8] Chan, T.F., Yan, L.T., Fang, S.Y. (2002). In-wheel permanent-magnet brushless DC motor drive for an electric bicycle. *IEEE Transactions on Energy Conversion*, 17(2): 229-233. <https://doi.org/10.1109/TEC.2002.1009473>
- [9] Huang, V.X. (2012). Modeling of exterior rotor permanent magnet machines with concentrated windings. Doctoral Thesis, Technische Universiteit Delft.
- [10] Jung, W.S., Lee, H.K., Lee, Y.K., Kim, S.M., Lee, J.I., Choi, J.Y. (2023). Analysis and comparison of permanent magnet synchronous motors according to rotor type under the same design specifications. *Energies*, 16(3): 1306. <https://doi.org/10.3390/en16031306>
- [11] Jusoh, L.I., Sulaiman, E., Bahrim, F.S., Kumar, R. (2017). Design comparison of inner and outer rotor of permanent magnet flux switching machine for electric bicycle application. In *IOP Conference Series: Materials Science and Engineering*. IOP Publishing, 226(1): 012129. <https://doi.org/10.1088/1757-899X/226/1/012129>
- [12] Kim, S.J., Park, E.J., Jung, S.Y., Kim, Y.J. (2017). Transfer torque performance comparison in coaxial magnetic gears with different flux-modulator shapes. *IEEE Transactions on Magnetics*, 53(6): 1-4. <https://doi.org/10.1109/TMAG.2017.2663429>
- [13] Zhu, Z.Q., Howe, D. (2000). Influence of design parameters on cogging torque in permanent magnet machines. *IEEE Transactions on Energy Conversion*, 15(4): 407-412. <https://doi.org/10.1109/60.900501>
- [14] Liu, X., Zhang, Z., Xiao, J., Xu, H. (2018). Comparison and analysis of electromagnetic characteristics of IPMSM with single and double layer PMs. *International Journal of Applied Electromagnetics and Mechanics*, 58(4): 483-496. <https://doi.org/10.3233/JAE-180032>
- [15] Dong, J., Huang, Y., Jin, L., Lin, H. (2016). Comparative study of surface-mounted and interior permanent-magnet motors for high-speed applications. *IEEE Transactions on Applied Superconductivity*, 26(4): 1-4. <https://doi.org/10.1109/TASC.2016.2514342>
- [16] Pu, T., Du, G., Tong, J., Huang, N., Li, N., Xu, W. (2021). Comparison of rotor strength of various rotor structures for ultra-high-speed permanent magnet synchronous motor. In 2021 IEEE 4th Student Conference on Electric Machines and Systems (SCEMS), Huzhou, China, pp. 1-6. <https://doi.org/10.1109/SCEMS52239.2021.9646110>
- [17] Sahebjam, M., Sharifian, B., Feyzi, M.R., Sabahi, M. (2019). Novel unified control method of induction and permanent magnet synchronous motors. *International Journal of Engineering*, 32(2): 256-269.
- [18] Ponnam, V.K.B., Swarnasri, K. (2020). Multi-objective optimal allocation of electric vehicle charging stations and distributed generators in radial distribution systems using metaheuristic optimization algorithms. *Engineering, Technology & Applied Science Research*, 10(3): 5837-5844. <https://doi.org/10.48084/etasr.3517>
- [19] Natarajan, S., Kasinathan, G. (2023). A hybrid MIP-CBO approach for loss minimization of the PMSM-fed electric vehicle drive system. *Engineering, Technology & Applied Science Research*, 13(6): 12278-12283. <https://doi.org/10.48084/etasr.6396>